

# Water Harvesting at the Single-Crystal Level

Adrian Fuchs,<sup>○</sup> Fabian Knechtel,<sup>○</sup> Haoze Wang, Zhe Ji, Stefan Wuttke, Omar M. Yaghi,\*  
and Evelyn Ploetz\*

Cite This: *J. Am. Chem. Soc.* 2023, 145, 14324–14334

Read Online

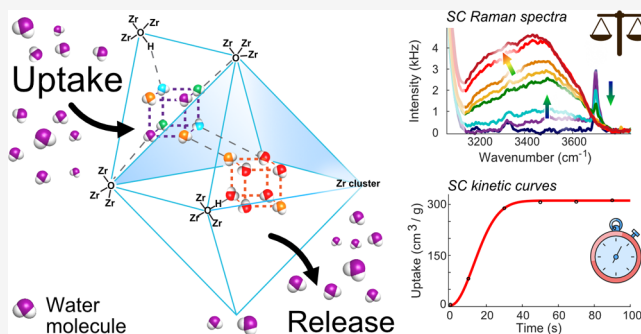
ACCESS |

Metrics & More

Article Recommendations

Supporting Information

**ABSTRACT:** Metal–organic frameworks (MOFs) have emerged as a class of porous materials with facile uptake and release of water, turning them into excellent substrates for real-world atmospheric water harvesting applications. The performance of different MOF systems was experimentally characterized at the bulk level by assessing the total amount of water taken up and the release kinetics, leaving the question behind of what the upper limit of the pristine materials actually is. Moreover, recent devices rely on fluidized bed reactors that exploit the harvesting capacities of MOFs at the single-crystal (SC) level. In this publication, we present a novel methodology based on Raman spectroscopy, for acquiring water adsorption isotherms and kinetic curves with a sub-micrometer resolution that provides valuable insights into the material behavior probing the pristine MOF at the SC level. We investigated isolated MOF-801 particles in situ and could dissect contributions of intra- and inter-particle effects on the water harvesting performance of MOF-801 via adsorption–desorption isotherms and kinetic curves. Using spontaneous Raman spectroscopy, we found an almost 20-fold faster uptake for the undisturbed crystalline material. Correlative imaging based on four-wave mixing and coherent anti-Stokes Raman scattering further localized the uptaken water inside MOF-801 and identified inter-particle condensation as the main source for the discrepancies between the performance at the bulk and SC level. Our studies determined an upper limit of around 91.9 L/kg<sub>MOF</sub>/day for MOF-801.



## INTRODUCTION

Knowing the upper limit of an intrinsic property for a material is critically important in realizing its full potential. For example, the determination of all the adsorptive sites in metal–organic frameworks (MOFs) has led to the design of structures with exceptionally high surface areas.<sup>1</sup> Recently, MOFs have been shown to be useful in harvesting water from desert air,<sup>2–10</sup> where the water productivity depends on how fast water can move in and out of the pores.<sup>4,11–14</sup> While such cycling kinetics of water sorption could be measured experimentally in bulk,<sup>2–4,6,10,15–19</sup> this is yet to be done on the single-crystal (SC) level, leaving unanswered the question of what is the upper limit of how much water can be harvested in a given time.

The uptake performance of porous materials is usually determined by measuring bulk properties using mass gravimetric methods<sup>3,8</sup> and described by the total uptake, the uptake mechanism (hence isotherm type), and the kinetic behavior. However, MOF materials feature—like all crystalline materials—diverse defect sites (Figure 1), resulting in the disruption of their crystallinity due to macropores, mechanical deformations, or inter-crystal growth. The latter leads to particles with multiple crystalline zones or amorphous areas.

In addition to defects (even if ideally grown), SCs interfere with each other's uptake behavior in multiple ways, such as (i)

shielding neighboring particles from adsorbing guest molecules in the surrounding airflow and, hence, reducing the accessibility to pores or (ii) by creating condensation pockets between them.<sup>20</sup> Measuring the performance of the sorbent material, without any interference of intra- and inter-particle effects, would require a spatially resolved quantitative method for monitoring the uptake.

Herein, we present a general strategy to quantitatively determine the water sorption isotherm and the kinetics of uptake and release within SCs. We developed an optical methodology based on Raman spectroscopy (Materials and Methods Section 1–2) to quantitatively determine SC isotherm and kinetic curves with sub-micron spatial resolutions. We chose MOF-801 in this study, an important and widely used MOF for AWH.<sup>2</sup> We found that for SCs, saturation in uptake is reached ~20 times faster than in the bulk.<sup>11</sup> This resets the upper limit for MOF-801 and indicates that water harvesting devices could produce up to 3.8 L of

Received: March 20, 2023

Published: June 23, 2023



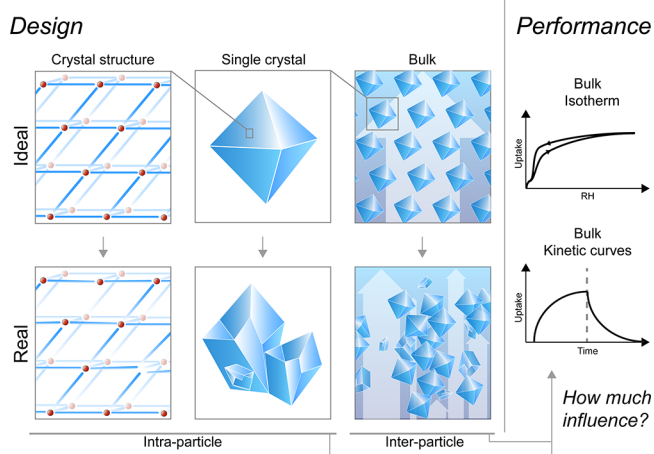


**Figure 1.** Design and performance evaluation of atmospheric water harvesting (AWH) MOF materials comparing the influence of intra- and inter-particle effects on the bulk performance of sorbent systems for an ideal (SC) and real (bulk) material.

water per hour per kilogram of MOF, a vast improvement over the previously reported 2.8 L per day per kilogram of MOF.<sup>4,11</sup>

## RESULTS AND DISCUSSION

**Monitoring the Water Uptake in MOF-801 Crystals via Raman Spectroscopy.** The structure of MOF-801 is formed by zirconium hydroxide oxide  $Zr_6O_4(OH)_4$  clusters with fumarate dianions in a *fcu* topology. We implemented

spontaneous Raman microscopy for the label-free, 3D characterization of the chemical composition and background-free detection of water inside MOF-801. The water signature (characterized by the broad OH-stretch vibration around  $3300\text{ cm}^{-1}$ ) and MOF-801 bands are well spectrally separable (Figure 2a). Hyperspectral Raman imaging (HRI) confirmed octahedral crystals with triangular surfaces and a diameter of about  $5\text{--}10\ \mu\text{m}$  (Figures 2b and S1, Type 1) and enabled us to position the crystals for probing the uptake performance of MOF-801 in the center of the particle. We employed the linear dependence of the Raman intensity with the number of scatterers to quantify water uptake in situ with a spatial resolution of  $\sim 270\text{ nm}$  provided by the confocal microscope. Therefore, the probed volume is significantly lower than the average MOF-801 crystal size, which allows us to image across crystals and within SCs.

First, we employed Raman spectroscopy to confirm the known mechanism of water uptake originally derived from SC-X-ray diffraction (XRD).<sup>2</sup> A detailed description of the model is given in Supplementary Note 1. We monitored the Raman signature of water in single MOF-801 crystals (Figure S2) with respect to the spectral position and shape of the OH-stretch vibration with increasing relative humidity (RH). MOF-801 features a multi-step mechanism for water uptake using binding sites in tetrahedral and octahedral cages within the asymmetric unit cell of MOF-801 (Figure 2c). In the dry state with no water molecules bound, only the Zr:  $\mu_3$ -OH stretch vibration of the metal-bound hydroxyl ligand at  $3682\text{ cm}^{-1}$  was detectable in the OH region (Figure 2c). This sharp, defined

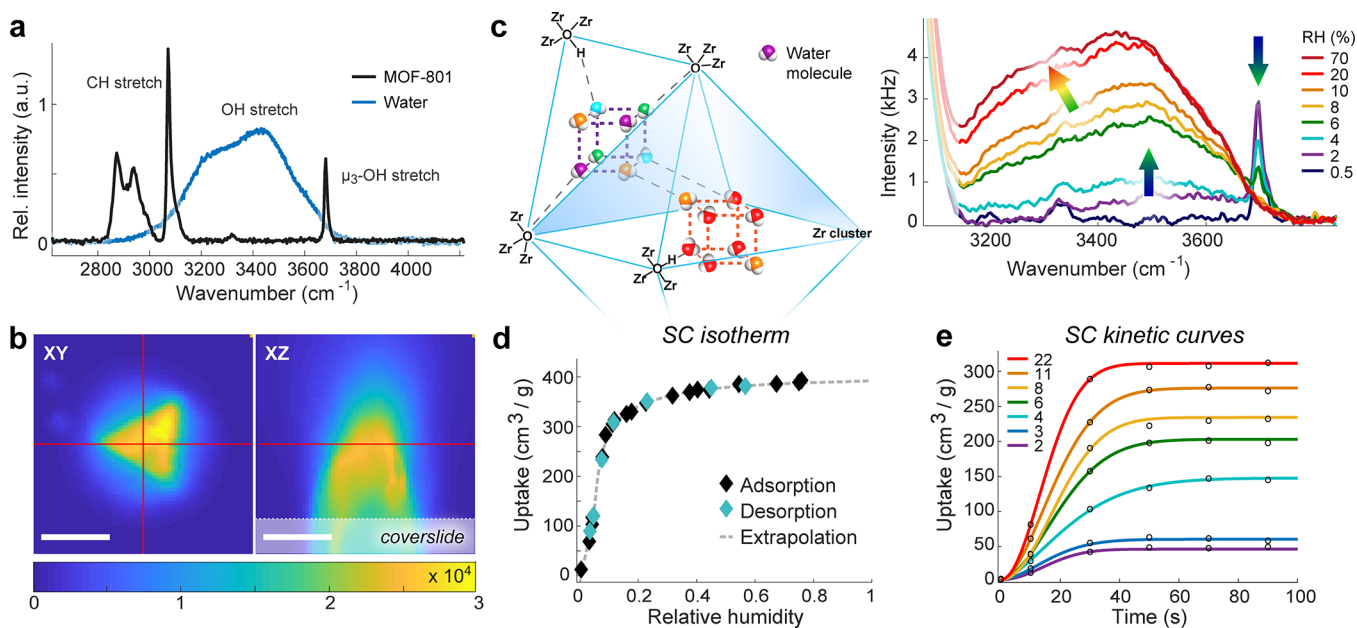


**Figure 2.** Water uptake in MOF-801 crystals monitored by Raman spectroscopy. (a) Raman spectra of dry MOF-801 and liquid, double-distilled water. (b) Raman image based on the  $C=C$  stretch vibration at  $1670\text{ cm}^{-1}$  in the XY and XZ plane showing an isolated single MOF-801 crystal. Red lines mark the measurement height and position for recording SC isotherms and kinetics. The white area shows the coverslide. The scanning range was  $16 \times 16\ \mu\text{m}^2$  with 70 pixels per line. Scale bar:  $5\ \mu\text{m}$ . (c) Raman spectra of MOF-801 at increasing RH confirm consecutive binding of water molecules in the tetrahedral (purple dotted cube) and octahedral (red dotted cube) binding sites of the crystal structure. The coloring of water molecules (starting from blue, purple, cyan, green, and orange to red) indicates the binding order according to the uptake mechanism for MOF-801 reported by SC-XRD.<sup>2</sup> Arrows indicate spectral changes between corresponding humidities. Abbreviations: Zr: zirconium; O: oxygen; H: hydrogen atoms. (d) Absolute water uptake of SC MOF-801 derived from the ratiometric Raman analysis at varying humidities. Adsorption (black) and desorption (cyan) are reversible. The dotted line indicates the underlying isotherm, extrapolated to 100% RH. (e) Kinetics of water uptake within the same crystal after exposure to selected RHs. The uptake saturates in less than 60 s. Colored lines represent single-step Avrami fits, and black dots show the data points.

resonance of this  $\text{Zr}(\mu_3\text{-OH})$  hydroxyl group gives clear evidence of the crystalline nature of the MOF particle and the absence of guest molecules. The binding of water molecules is expected to occur in the tetrahedral binding pocket to  $\text{Zr}(\mu_3\text{-O})$  units (purple water molecules). Indeed, we observed at 2% RH a rise in the broad OH-stretch of water molecules between 3400 and 3700  $\text{cm}^{-1}$ , while the  $\text{Zr}(\mu_3\text{-OH})$  sites were unaffected and showed an identical Raman intensity as in the dry state (Figure 2c). Between 2 and 6% RH, water also adsorbed at the  $\text{Zr}(\mu_3\text{-OH})$  sites (turquoise water molecules), diminishing the vibration of the free  $\mu_3\text{-OH}$  stretch band at 3682  $\text{cm}^{-1}$  until it vanished at 8% RH. The Raman signature between 3200 and 3700  $\text{cm}^{-1}$  continued to grow due to molecules bound to secondary adsorption sites (green and orange water molecules in Figure 2c) that start forming networks, as expected for water dimer formation.<sup>21–23</sup> The rise in intensity was accompanied by a shift of the OH peak maximum to lower wavenumbers with increasing uptake of water due to network formation via hydrogen bonding. SC adsorption experiments of heavy water by MOF-801 showed an identical uptake mechanism (Supplementary Note 2) following the same uptake steps for  $\text{D}_2\text{O}$  via binding to the Zr cluster, consecutive nucleation, and pore filling, accompanied by a shift to lower wavenumbers of the  $\text{Zr}(\mu_3\text{-OD})$  stretch vibration) with increasing uptake of saturated guest molecules. After saturation of the tetrahedral binding sites, the octahedral binding pockets started to be occupied until saturation was reached (red water molecules). Saturation starts above 20% RH with only a small amplitude increase up to 70% RH. With increasing RH, every new water molecule is further away from the metal clusters. The spectral shape of the OH-stretch water peak in MOF-801 starts resembling the Raman signature of liquid water (Figures 2c and S3) as water guest molecules fill up the pores of MOF-801 gradually. This finding suggests that water molecules do not experience the confinement of the framework at large RHs any longer, which was recently also found for the Co-MOF  $\text{Co}_2\text{Cl}_2\text{BTDD}$ .<sup>23</sup> The humidity-dependent Raman spectra match well with the published uptake mechanism of MOF-801, validating the spectroscopic platform we have developed.

Next, we exploited our newly developed, theory-supported method to quantify the adsorbed water at the SC level (Methods Section 2 and Supplementary Note 3). Starting from the recorded Raman spectra, the volume of water uptake  $\frac{V_{\text{H}_2\text{O}}}{m_{\text{MOF}}}$  (in  $\text{cm}^3/\text{g}$  of MOF) can be expressed via the density of the water-free host material  $\rho_{\text{MOF}}$  and the ratiometric expression  $\frac{A_{\text{OH}}}{A_{\text{CH}}}$  linking the Raman intensity of the OH-stretch vibration of water to the CH-stretch vibration of MOF-801.

$$\frac{V_{\text{H}_2\text{O}}}{m_{\text{MOF}}} = \frac{A_{\text{OH}}}{A_{\text{CH}}} \cdot \frac{1}{\rho_{\text{MOF}}} \cdot \Gamma \quad (1)$$

The scaling factor  $\Gamma$  can be approximated as a material constant (Supplementary Note 3.3) and experimentally calibrated and theoretically modeled from the predicted number of water molecules  $N_{\text{H}_2\text{O}}(\text{RH})$  in the asymmetric unit cell of MOF-801 at a given RH. Knowing both the host density and scaling factor, the ratiometric ratio of OH to CH stretch Raman intensity directly relates to the absolute amount of adsorbed water molecules.

We subsequently evaluated the inherent material performance of MOF-801 for taking up water without the interference

of intra- or inter-particle effects by taking a series of Raman spectra for the inside of homogeneous SCs. These were recorded as a function of RH (i.e., as isotherm curves) or as a function of the time after exposure to a given humidity (i.e., kinetic curves). Figure 2d displays the SC isotherm for MOF-801 at 23.3 °C probed within a sub-micron region of the crystal. The isotherm is characterized by a three-step behavior: after a steep uptake increase below ~8% RH, it features a second phase with slower adsorption behavior until 20% RH and slow saturation in the last phase above 20% RH. In contrast to bulk experiments,<sup>2</sup> no hysteresis could be observed, as expected for regular SCs with uniform pore size. Monitoring the temporal behavior of water uptake by MOF-801 at different RHs between 2 and 20% RH (Figure 2e) shows a nearly instantaneous uptake within the first tens of seconds and the built-up of a constant plateau that agrees well with the total amount of water observed in the SC isotherm. This rapid uptake behavior is independent of the measurement position in MOF-801 crystals with a diameter below 10  $\mu\text{m}$  (Supplementary Notes 4 and 5). By modeling the kinetics using an Avrami model,<sup>24,25</sup> we found a saturation time of around ~50 s (Supplementary Note 1.2).

**Influence of Defects and Inter-Particle Effects at the SC Level.** For water harvesting applications, MOF-801 is usually grown in monocrystalline, regular SCs (Type 1) as observed, for example, by scanning electron microscopy (SEM; Figure 3a).<sup>2</sup> However, within the same synthesis batch, we also found MOF-801 particles without sharp edges (Type 2; Figure 3b), accounting for about 10% of the total particles. While regular crystals possess strongly reflecting surfaces with defined triangular shapes, Type 2 crystals display a complex inner structure as observed by bright-field microscopy (BF; Figure 3c,d). We verified the associated, higher level of defects by four-wave mixing (FWM) imaging, which is susceptible to defect level and irregularities.<sup>26</sup> In contrast to the regularly formed, homogeneous MOF-801 crystals, we found inhomogeneous substructures in defect-rich particles (Figure 3d) with localized, enhanced FWM signals indicating open metal sites inside the material.<sup>26</sup> SC-XRD on Type 1 and 2 crystals further confirmed the monocrystalline and polycrystalline nature of the material (Supplementary Note 6), respectively. While Type 1 crystals possessed the expected cubic unit cell with space group<sup>2</sup>  $\text{Pn-3}$ , Type 2 particles were composed of multiple MOF-801 unit cell patterns with different orientations in the same crystal, hence representing defect-rich crystals with sub-crystallization zones.

Next, we investigate how intra-particle features in defect-rich particles influence the SC water uptake performance compared with monocrystalline MOF-801. Figure 3e depicts the mean SC isotherm of regular SCs (blue; standard deviation as blue shade; Figure S4) at 23.3 °C. We found a type IV isotherm with a clear step around 7% RH, a fast saturation below 20% RH, and a maximum uptake of about 379  $\text{cm}^3/\text{g}$  ( $\pm 16.5 \text{ cm}^3/\text{g}$ ) at ~77% RH.

While the mean isotherm of defect-rich particles (Figure 3e, orange) resembled the overall performance of regular crystal isotherms, it displayed three major differences: (i) First, the standard deviation was significantly higher, reflecting the high variance of the underlying defects in the selected particles. (ii) Second, a higher uptake at low RH was seen for isotherms in Type 2 particles. The accompanying shift of the isotherm step toward lower RH confirms a higher amount of primary water molecules in the structure and missing cluster defects, as



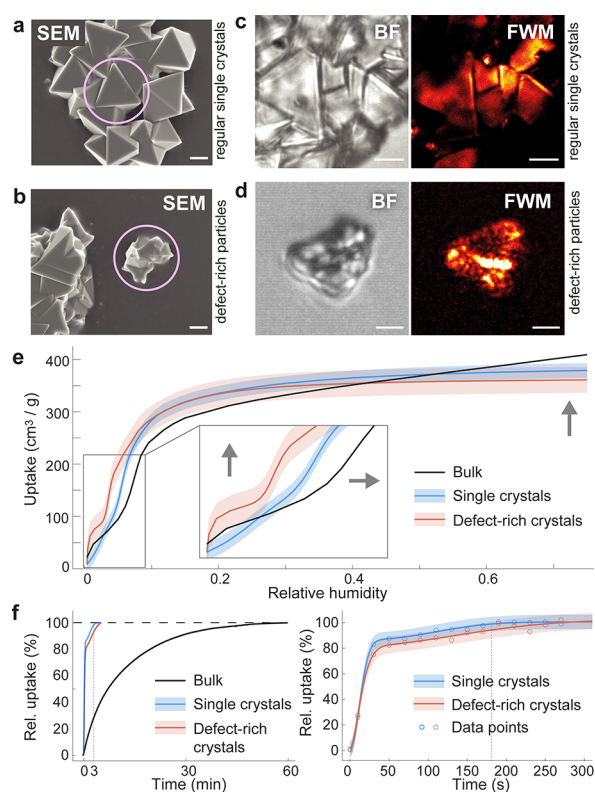


**Figure 3.** Performance of single mono- and polycrystalline MOF-801 particles on SC isotherms and uptake kinetics. (a–b) SEM images of (a) regular crystals and (b) polycrystalline particles. (c,d) BF and FWM images of (c) regular crystals and (d) polycrystalline particles. Measurement details are given in Material Section 5. (e) Isotherms of the bulk, regular, and defect-rich MOF-801 crystals. The colored lines represent the mean fit curve of regular ( $N = 7$ ) and defect-rich ( $N = 5$ ) crystals (Figure S4). The shaded areas represent the corresponding standard deviation. (f) Bulk and average SC adsorption kinetic of dry MOF-801 ( $N = 5$ ) after exposure to nitrogen with 8% RH, described by a customized Avrami fit function. While a thin layer of bulk material needs about 1 h until saturation, SCs saturate in 3–4 min (left panel). Dotted lines mark the 3 min time point. Even defect-rich particles take up >80% of the total amount in less than 60 s (right panel). Circles mark the center of the 20 s long detection window per point. The standard deviation (shaded area) was derived per data point (Figure S5). Scale bars: 5  $\mu\text{m}$ .

observed by FWM imaging. (iii) Third, the average maximum uptake is decreased compared with regular crystals, meaning that the inner surface per volume of defect-rich particles was found to be lower.

Overall, the SC isotherms look similar to the bulk, although both measuring techniques (mass gravimetry and spectroscopy) are fundamentally different. The bulk isotherm showed a higher uptake compared to the regular SC isotherm at very low RH, indicating open metal sites as observed for defect-rich particles. Below 10% RH, the bulk isotherm rises less steeply than the SC isotherm, causing a shift of the inflection point toward higher RH. Above 10% RH, the SC and the defect-rich isotherm both show a distinct saturation, while the uptake still increases linearly in bulk. At RH over  $\sim 60\%$ , this results in more water uptake by the bulk material than SCs. However, water adsorbed in this regime is not accessible for harvesting applications at low humidity. Since the pores are already filled, this difference is attributed to inter-particle water condensa-

tion—a contribution that cannot be quantified by conventional bulk experiments.

Besides, the bulk differs significantly from the SC in kinetic behaviors (Figure 3f). While the SC water uptake was equilibrated within less than 3 min after a change in RH, the uptake in bulk equilibrated after 1 h. The kinetic response of dry, regular MOF-801 crystals (8% RH) revealed a fast uptake, reaching >85% of its capacity within the first 60 s. The datasets were approximated by a dual-step Avrami model (Supplementary Note 1.2; Figure S5). It reveals a second uptake step between 100 and 200 s, probably due to subsequent filling of the octahedral binding sites in MOF-801. The kinetic behavior of Type 2 particles (Figure 3f; orange curve) followed the Type 1 curve very closely. When modeling the condensation of water within MOF-801 by a dual-step Avrami fit, more than 80% uptake was found to occur within the first minute, while the successive filling process was observed from 100 to 200 s. Overall, water uptake by Type 2 particles was found to happen slower than by Type 1 crystals. This might be caused by the complex inner structure, hindering the fast transport to the inside of the particles. It could also be that defect sites on the peripheral regions of the particle spawn fast water clustering, which blocks the diffusion of water molecules further inside.<sup>27</sup> However, when considering the  $\sim 20$  times difference in equilibration time, both micron-sized, crystalline systems possess much faster kinetics than the composed bulk system.

### Influence of Inter-Particle Condensation on Water Harvesting.

In bulk, water can condense in the inter-particle space between crystals contributing additionally to the uptake. To investigate the influence of interparticle condensation, we combined FWM and coherent anti-Stokes Raman scattering (CARS) imaging and visualized the morphology and position of MOF-801 compared to the distribution of uptaken water. FWM monitors the distribution of the MOF-801 material and especially open metal sites,<sup>26</sup> while CARS maps the local water distribution. We first visualized the water distribution of Type 2 MOF-801 particles of the large crystal batch and found water mainly in the inter-particle space (Figure S6a,b). Since the amount of defective Type 2 particles among the large monocrystalline crystals (Type 1) were very low, we modeled those by aggregates of monocrystalline crystals of 0.5–1  $\mu\text{m}$  in diameter for CARS and FWM imaging. Figure 4a–d (Supplementary Note 7) summarizes the results of correlative FWM/CARS experiments on cyclic water uptake in polycrystalline MOF-801 clusters. The particles were first localized via BF (Figure 4a) and FWM microscopy under dry conditions (Figure 4b; red hot). Next, the CARS signal (Figure 4b; blue) of water was recorded at 60% RH to visualize the water distribution across the MOF particles. The water appeared again mostly anti-correlated to the FWM signal, showing the liquid water between and around the crystals. To investigate how reversibly inter-particle water binds to polycrystalline particles, we repeated the CARS experiment in the same field-of-view under three different conditions: (1) after drying the MOF particles for 10 min with  $\text{N}_2$ , (2) after exposure to 60% RH for 10 min, and (3) after drying the particles again. CARS microscopy revealed (Figure 4c) that polycrystalline aggregates hardly released any water. On the contrary, the water content between the particles even grew during the cycling experiments for most of the particles (Areas I and II in panel b, Figure 4d). Once adsorbed to the MOF-801 framework, the water turned out to be inaccessible to water harvesting applications.

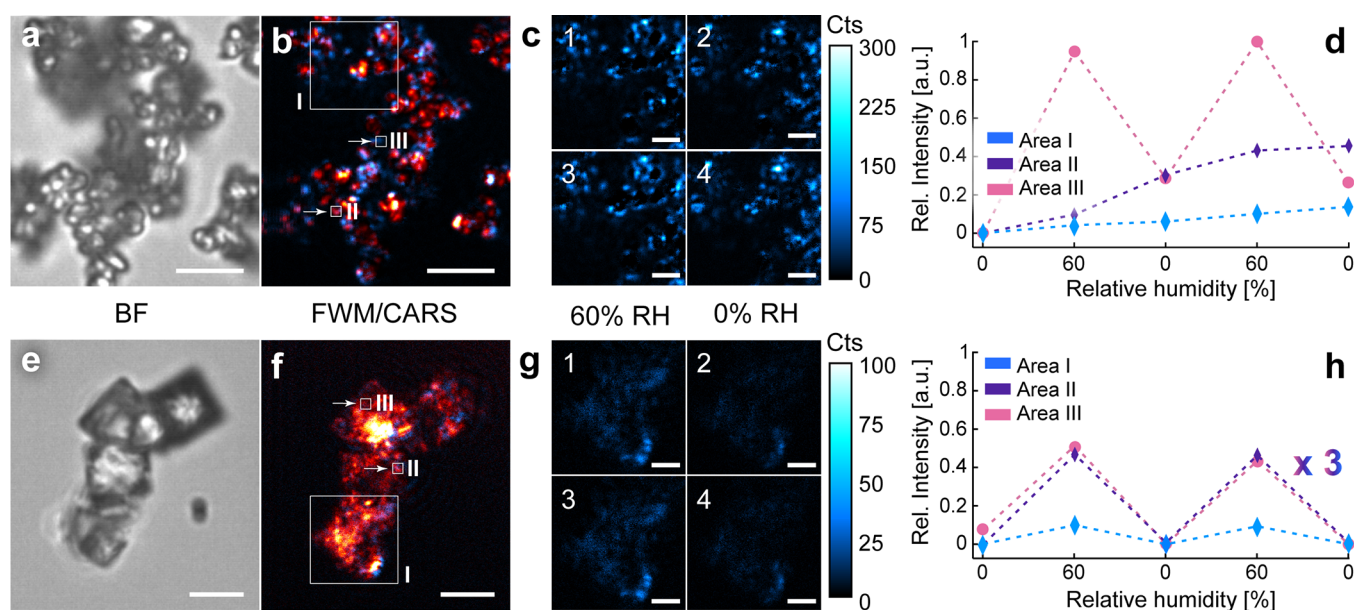


**Figure 4.** Influence of inter-particle effects in MOF-801. Correlative FWM and CARS imaging highlight the difference in water uptake for defect-rich, polycrystalline particles (a–d; top) and monocrystalline MOF-801 (e–h; bottom). (a) BF image of amorphous, polycrystalline particles. (b) Overlay of FWM and CARS images. FWM (red hot) maps the distribution of particles in the field of view. CARS (blue overlay) shows a high water content, which is heterogeneously distributed among the particles. (c) CARS images probing the water signature at  $3400\text{ cm}^{-1}$  reveal a 3–4 fold larger water uptake compared to regular crystals (Figure 4g), which is not released. (d) Amount of adsorbed water by MOF-801 for different areas marked in (b) after two cycles of exposure to humidity and drying. The uptake and release behavior is highly heterogeneous. The majority (areas 1 and 2) shows a steady increase in water. Only selected areas (e.g., area 3) show a cyclic uptake and release behavior. (e) BF image shows 7 intergrown MOF-801 crystals. (f) Overlay of FWM image (red) showing the particle position and CARS image (blue) showing the water distribution within the material at 60% RH. Water is homogeneously distributed. (g) CARS image probing water at  $3400\text{ cm}^{-1}$ . Zoom-in on area 1 marked in (f) after cyclic exposure to 60% RH and drying afterward (indicated by numbers 1 to 4 with 1 and 3 being at 60% RH and 2 and 4 being at  $\sim 0\%$  RH). (h) Relative water content for different areas marked in (f) shows a uniform and synchronous uptake and release. The signal is multiplied by a factor of 3 for better visibility. Scale bars:  $5\ \mu\text{m}$ .

Correlative FWM/CARS experiments on cyclic water uptake in monocrystalline MOF-801 (Type 1), however, revealed a synchronous uptake and release of water (Figure 4e–h; Supplementary Note 7). The intergrown, monocrystalline particles showed little inter-crystalline water condensation between regular crystals but a uniform distribution of water which is about 3-fold lower than for polycrystalline particles (Figure 4g,h). They show a synchronous uptake and release when cycling between 0 and 60% RH (Figure 4g,h), which is identical to isolated MOF-801 crystals (Figures 2e and S6c). Overall, water uptake in regular, monocrystalline MOF-801 crystals is highly reversible, while for polycrystalline or small MOF-801 crystals, inter-particle condensation with permanent water enclosures dominates. This finding also explains the increased amount of water taken up by bulk samples and the hysteresis observed in the isotherms of the bulk (Figure S6d), which is absent in the isotherms of regular SCs (Figure 2d).

For monocrystalline MOF-801 (Type 1), the desorption time of SCs is in the same regime as the adsorption (Figure 5a). The inherent cycle time for MOF-801 is significantly shorter than the cycle time employed in water harvesting devices that suffer from inter-particle contributions. To address the maximum harvesting capabilities of pristine MOF-801 crystals, we selected a regular SC and cycled the RH between 0 and 8% with a cycle time of 160 s (Figure 5b). The sample was first completely dried with nitrogen (Methods Section 3). Next, the RH of the gas stream over the sample was changed from 0 to 8% RH (or back) every 80 s, while the uptake was monitored. The first desorption did not return to the ground level at  $t = 0$  s, which could be caused by primary-bound water

molecules that cannot desorb on the selected time scale. Over five cycles, we found a total difference in relative uptake (maximum–minimum per cycle) of  $851 \pm 13.3\text{ cm}^3$  per  $\text{g}_{\text{MOF}}$ , which can be extrapolated to a potential harvest of even  $\sim 170\text{ cm}^3$  per g MOF every 160 s or  $91.91 \pm 1.44\text{ L}$  per  $\text{kg}_{\text{MOF}}$  per day (Figure 5c), respectively, for an isolated MOF-801 crystal of about  $15\ \mu\text{m}$  in diameter.

In comparison to the literature, MOF-801 was implemented into a water harvesting device to test practical water harvesting cycling (WHC).<sup>28</sup> It produced 100 g of water per kg of material, however, requiring a day-and-night cycle. Similarly, Kim et al. reported a theoretical harvest of  $\sim 250\text{ g}$  per  $\text{kg}_{\text{MOF}}$  per day.<sup>4,11</sup> Faster WHC (36 and 26 min) was achieved by fluidization of the MOF particles, but requiring active heating and cooling,<sup>29</sup> in contrast to the experiments in this work (see Supplementary Note 8). The remarkable time difference between WHC on the SC level and literature values indicates the vast potential of achieving the upper limit of the material. This corresponds to harvesting 360–920 times more water compared to currently available devices without active heating. Although the extrapolated harvesting yield for a single MOF-801 might represent a theoretical value for the uptake limit and speed in practical applications, it highlights the importance of synthesis procedures and thought-out technical implementations in order to exploit the full potential of MOF-801 for water harvesting. Our results show that this striking difference can be, for the most part, attributed to the influence of permanently bound inter-crystalline water. This contribution can be minimized by increasing the crystal size to the 10–20  $\mu\text{m}$  regime (where intra-particle diffusion is still neglectable)



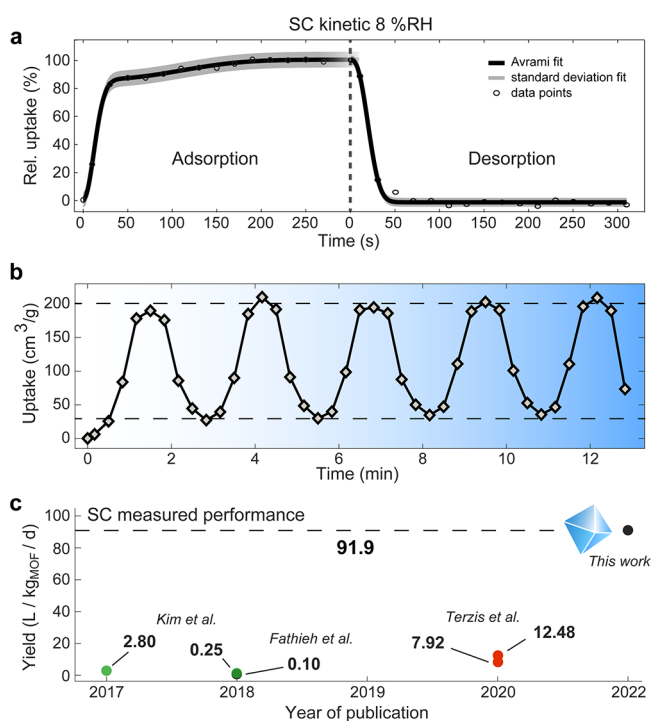


**Figure 5.** SC sorption behavior of MOF-801 particles at the SC level. (a) Time course of water attachment after switching from 0 to 8% RH and back on a time window of 300 s each. Timepoint 0 represents the exposure to the altered RH. Both data sets represent the mean and standard deviation over 5 crystals. (b) Relative SC uptake when switching the RH that surrounds the sample between 0 and 8% RH every 80 s. (c) Overview of published water yields in MOF-801 in bulk compared to the relative SC uptake in (d) ( $91.91 \pm 1.44$  L/kg<sub>MOF</sub>/d, dotted line): Kim et al. (ref 4, 11; green) reported a potential yield for a solar-powered device at 20% RH of 2.8 L/kg<sub>MOF</sub>/d in 2017 and a prototype in 2018, which could produce 0.25 L/kg<sub>MOF</sub>/d at 10–40% RH. At the same time, Fathieh et al. (ref 28; black) reported a prototype with a capacity of 0.1 L/kg<sub>MOF</sub>/d tested in the desert with no additional cooling and only ambient sunlight. Terzis et al. (ref 29; red) applied active heating and cooling to a fluidized MOF-801 powder to enable fast cycling times with 7.92 (at 18% RH) and 12.48 L/kg<sub>MOF</sub>/d (at 39% RH).

and/or by employing engineering schemes based on fluidized-bed reactors which rely on water uptake in isolated monocrystalline MOF-801 particles. SC isotherm and kinetic experiments allow, for the first time, to evaluate the degree of deterioration in water sorption performance due to a “contamination” by poorly crystalline material and can, hence, guide future development of sorption material applications.

## CONCLUSIONS

We have demonstrated a methodology based on in situ Raman spectroscopy for measuring qualitative and quantitative water sorption with sub-micron resolution. By monitoring and understanding the intra- and inter-particle contribution of water uptake via adsorption–desorption isotherm and kinetic curves in MOF-801 at the SC level, we found a striking difference in sorption behavior between SCs and the bulk material. Before this work, it was assumed that the measured bulk sample was representative for each crystal, which is in turn representative of a unit cell, when applying sorption isotherms, although crystals were not created equally nor possessed

identical characteristics, such as size, morphology, or defect level. By measuring cyclic water sorption at the SC level, which is the most intrinsic state of the solid material, we determined the upper limit for MOF-801 with a minimum cycle time below 3 min. This surprisingly fast cycle time enables a potential harvest of  $\sim 3.8$  L water per hour per kilogram of MOF, a significant improvement over the previously estimated 2.8 L per day.<sup>4,11</sup> Therefore, our approach could help to reveal the upper limit of a material’s inherent property to push technology advancement.

## MATERIALS AND METHODS

**Hyperspectral Raman Imaging at a Controlled Relative Humidity.** Static and dynamic Raman spectroscopy measurements were carried out on a home-built, confocal, multi-modal microscope using a 532 nm CW laser source (Samba 100 04–01, Cobolt GmbH).<sup>26</sup> If not mentioned otherwise, the power density was 58.5 mW/ $\mu\text{m}^2$  for all measurements (cf. Supplementary Note 8). Spectra were recorded between 2300 and 4215  $\text{cm}^{-1}$  probing the CH-stretch region of the MOF-801 material, and the OH-stretch vibrations of adsorbed water molecules, if not mentioned otherwise. The spatial resolution of the Raman mapping experiment was 0.27  $\mu\text{m}$  in the lateral and 0.74  $\mu\text{m}$  in the axial direction for a 60 $\times$  water-immersion objective lens (1.2 NA). The scattered light at the sample was collected in epi-detection using a spectrometer (Kymera 328i, Andor Solis) equipped with a 300 lines/mm grating and a 512  $\times$  512 pixel emCCD camera (iXon 897, Andor Solis). This instrumental configuration enables a spectral resolution of  $\sim 15$   $\text{cm}^{-1}$ . The spectral acquisition was controlled by *Andor Solis for Imaging V4.30* (Oxford Instruments). For image acquisition, areas with 500 nm step-size were raster-scanned, while full Raman spectra were recorded at each pixel of the image in multitrack mode. The acquisition time per pixel was set to 5 s.

For monitoring adsorbed water molecules in MOF-801 in situ, we installed a RH control unit (Figure 6a) on the confocal setup. The MOF sample is located in a channel slide ( $\mu$ -Slide I Luer, Ibidi) on top of the XYZ scanning stage of the microscope and connected to the flow system. Dry nitrogen serves as the reference and carrier gas for extracting water molecules from the MOF materials through constant flow. A three-way vault can switch between this drying line and the “wet line” containing nitrogen with a specific RH. The latter can be adjusted by the flow ratio regulated by two mass flow controllers (MFC, D-6311-FGD-33-AV-99-0-S-DR, Wagner Mess- und Regeltechnik GmbH): the nitrogen in the “wet line” is enriched with water vapor by diffusing through a double-distilled, water-filled vessel. The RH is controlled directly after mixing and at the sample chamber, as marked by RH in Figure 6a. The laboratory temperature was set to 23.3  $^{\circ}\text{C}$ , and the total mass flow was held constant at 1 standard liter nitrogen per minute for all experiments.

**Quantification of Water Uptake.** The local uptake and distribution of water were quantified based on the linear dependence of Raman scattering on the number of scattering molecules in the confocal volume (Supplementary Note 3). To ensure that water is evenly distributed in uniformly grown MOF-801 crystals, we first used hyperspectral Raman imaging (HRI) within a region of interest and recorded Raman spectra at each pixel. We visualized the water content in MOF-801 crystals first by univariate data analysis and derived the Raman intensity  $A_{\text{OH}}$  of the OH stretch vibration of water between 3145 and 3665  $\text{cm}^{-1}$  as a function of the position within the crystal

$$A_{\text{OH}}(x, y) = \int_{3145 \text{ cm}^{-1}}^{3665 \text{ cm}^{-1}} I_{\text{Raman}}(\tilde{\nu}, x, y) d\tilde{\nu} \quad (2)$$

Figure 6b depicts an exemplary water distribution at  $\sim 38\%$  RH. The apparent hexagonal shape of the crystal clearly confirms the sectioning capabilities of HRI and the correct positioning for imaging the particle: the image plane was successfully selected at around 50% height of the octahedral crystal (Figure S1) for monitoring the water content inside the crystal center. The HRI image shows a continuous

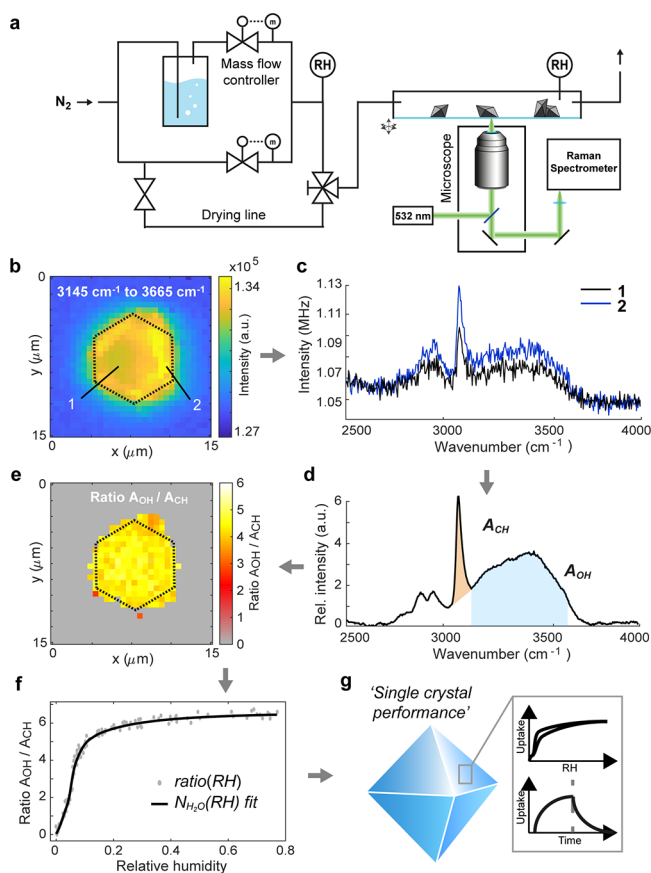


**Figure 6.** Quantification of water uptake in MOF-801 at the SC level by Raman spectroscopy. (a) Schematics of the micro-spectroscopy setup with the unit for controlling the RH over the sample. RH: RH measuring stations. (b) Univariate analysis of a hyperspectral Raman data set in the water OH-stretch region reveals an irregular water distribution in a regular SC of MOF-801. Crystal border at the measurement plane is indicated as dotted line. Raman mapping was carried out at 5 s integration time. The scanning range was  $20 \times 20 \mu\text{m}$  with 40 pixels per line. (c) Raman spectra of selected pixels marked in (a). (d) Background-corrected, mean spectrum over all pixels inside the crystal border. The strength of the CH- (orange) and the OH-stretch vibration (blue) is indicated as area under the graph. (e) The ratiometric representation  $A_{\text{OH}}/A_{\text{CH}}$  of the HRI data set in (a) shows a uniform water distribution. (f) Ratio  $A_{\text{OH}}/A_{\text{CH}}$  at varying RHs between 0 and 77% RH recorded for 7 regular SCs (gray points) allows for determining the number of water molecules per unit cell, i.e.,  $N_{\text{H}_2\text{O}}(\text{RH})$ . (g) Schematic of the SC performance methodology.

water distribution throughout the whole crystal with apparently increased water content at the surface boundaries, in addition to an intensity gradient from left to right. This apparent increase at the edges would indicate that saturation inside the crystal would not have been reached yet, even after 1 h of equilibration at  $\sim 38\%$  RH. For a regularly shaped crystal, we would expect an even distribution of adsorbed water per MOF material within minutes due to fast intracrystalline diffusion,<sup>20</sup> contrary to the experimental findings. Deviations in apparent water uptake are caused by a combination of light scattering at the edges and a varying amount of the MOF material inside of the detection volume due to defects and the 3D nature of the particles. Both effects lead to a variation in local excitation power and detection efficiency, an incomplete filling of the confocal volume, and concomitantly to a change in absolute amplitude of the recorded Raman spectra, as, for example, seen for areas within the interior (Position 1) and at the edge (Position 2) in MOF-801 (Figure 6c). To prevent any influence of these effects on

the quantification of the water uptake in MOF-801, we introduced a ratiometric approach that quantifies the amount of detected, water-associated OH-stretch intensity in comparison to the observed CH-stretch signal reporting on MOF-801 and hence the amount of the surrounding host material present. Here, the water uptake relates not to  $A_{\text{OH}}$  alone but to the ratio of  $A_{\text{OH}}/A_{\text{CH}}$ .<sup>30</sup> Figure 6d shows the background-corrected, mean spectrum over all pixels inside the crystal. The strength of the OH-stretch band  $A_{\text{OH}}$  is marked in blue and that of the CH-stretch  $A_{\text{CH}}$  is marked in orange. To correct against the spectral overlap between the water-based OH-stretch and MOF-801-associated CH-stretch resonance below  $3150 \text{ cm}^{-1}$ , modeling and deconvolution of the water peak from the MOF signature (Supplementary Note 3.2) were employed, resulting in the area marked in orange. Using the ratiometric representation, i.e., when plotting the peak ratio  $A_{\text{OH}}/A_{\text{CH}}$  as a function of position, the interior displays an even signal (Figure 6e), representing the expected uniform, saturated uptake of water inside the crystal. To convert the ratiometric Raman ratio into a quantitative measure, i.e., into water volume per mass of MOF-801, three interrelations need to be considered (see Supplementary Note 3 for a detailed description):

(1) The uptake can be related to the density of water  $\rho_{\text{H}_2\text{O}}$ , the respective molecular weight  $M_w$ , as well as the amount of material  $n_x$  in the confocal volume and hence the Raman intensity of the OH- and CH-stretch vibration

$$\frac{V_{\text{H}_2\text{O}}}{m_{\text{MOF}}} = \frac{n_{\text{H}_2\text{O}} \cdot \frac{M_{\text{H}_2\text{O}}}{\rho_{\text{H}_2\text{O}}}}{n_{\text{MOF}} \cdot M_{\text{MOF}}} = \frac{A_{\text{OH}}}{A_{\text{CH}}} \cdot \frac{c_{\text{OH}}}{c_{\text{CH}}} \cdot \frac{M_{\text{H}_2\text{O}}}{\rho_{\text{H}_2\text{O}} \cdot M_{\text{MOF}}} \quad (3)$$

The latter formula takes into account that the detected intensities of both Raman resonances  $A_x$  are proportional to the quantity of guest and host species

$$n_{\text{H}_2\text{O}} = c_{\text{OH}} \cdot A_{\text{OH}} / N_A \quad (4a)$$

$$n_{\text{MOF}} = c_{\text{CH}} \cdot A_{\text{CH}} / N_A \quad (4b)$$

(2) The conversion factors can be determined either experimentally or theoretically. Experimental calibration was carried out in pure water and a dry MOF-801 material. Knowing the density of the host and guest material allows for calculating the number of Raman active species in the confocal volume in the first step, irrespective of the absolute Raman intensities. The conversion factors of dry MOF-801 and water under excitation intensity would amount to

$$c_{\text{OH}} = \frac{n_{\text{H}_2\text{O,cal}}}{A_{\text{OH,cal}}} = \frac{\rho_{\text{H}_2\text{O}} \cdot V_{\text{confocal}}}{A_{\text{OH,cal}} \cdot M_{\text{H}_2\text{O}}} \quad (5a)$$

$$c_{\text{CH}} = \frac{n_{\text{MOF,cal}}}{A_{\text{CH,cal}}} = \frac{\rho_{\text{MOF}} \cdot V_{\text{confocal}}}{A_{\text{CH,cal}} \cdot M_{\text{MOF}}} \quad (5b)$$

with  $A$  referring to the peak strength of the OH- or CH-stretch vibration for the host and guest material. When combining eqs 4–5, the expression for water uptake shortens to

$$\frac{V_{\text{H}_2\text{O}}}{m_{\text{MOF}}} = \frac{A_{\text{OH}}}{A_{\text{CH}}} \cdot \frac{A_{\text{CH,cal}}}{A_{\text{OH,cal}}} \cdot \frac{1}{\rho_{\text{MOF}}} \quad (6)$$

For identical measurement conditions of the calibration measurements, the ratio  $\frac{A_{\text{CH,cal}}}{A_{\text{OH,cal}}} = \Gamma$  of calibrated Raman intensities remains constant and can be treated as a scaling factor

$$\frac{V_{\text{H}_2\text{O}}}{m_{\text{MOF}}} = \frac{A_{\text{OH}}}{A_{\text{CH}}} \cdot \Gamma \cdot \frac{1}{\rho_{\text{MOF}}} \quad (7)$$

As laid out in Supplementary Note 3, the measurement conditions for calibrations of host and guest molecules-associated scaling factors differ due to variations in excitation intensity induced by scattering in

the detection volume. While no polarization dependency in MOF-801 was found for the CH- and the OH-stretch Raman peak (Figure SN3.2), we need to incorporate the reduction in excitation power and hence linearly decreased the Raman signature of the detected CH-stretch vibration and adopt the experimental scaling factor to

$$\Gamma_{\text{exp}} = \frac{A_{\text{CH,cal}}}{A_{\text{OH,cal}} \cdot L_{\text{scatter}}} \quad (8)$$

We estimated the average scattering loss  $L_{\text{scatter}}$  on MOF-801 compared to transparent water alone by determining the integrated transmission intensity of broadband white-light via bright-field microscopy (Figure SN3.3). We experimentally obtained the loss parameter for MOF-801 to be  $0.5651 \pm 0.0884$  and the experimental scaling factor  $\Gamma_{\text{exp}}$  as  $0.0837 \pm 0.0131$ .

(3) Since the experimental determination of  $\Gamma$  is challenging, we further modeled the number of water molecules in the asymmetric unit cell of MOF-801 as a function of the RH  $N_{\text{H}_2\text{O}}(\text{RH})$  based on the water uptake mechanism in MOF-801.<sup>2</sup> Modeling by an adapted Klotz model revealed that the volume water uptake (in  $\text{cm}^3/\text{g}$  MOF) and RH  $N_{\text{H}_2\text{O}}$  are related by a linear scaling factor of 8.22 (Supplementary Note 1.2).

$$\frac{V_{\text{H}_2\text{O}}}{m_{\text{MOF}}} = N_{\text{H}_2\text{O}}(\text{RH}) \cdot 8.22 \quad (9)$$

Knowing that the ratio  $A_{\text{OH}}/A_{\text{CH}}$  describes the uptake as a function of RH while being proportional to the number of water molecules  $N_{\text{H}_2\text{O}}(\text{RH})$  by a constant factor  $f_{\text{fit}}$

$$\frac{A_{\text{OH}}}{A_{\text{CH}}} = N_{\text{H}_2\text{O}}(\text{RH}) \cdot f_{\text{fit}} \quad (10)$$

we can theoretically derive an expression for the scaling factor  $\Gamma_{\text{th}}$  (insert eqs 9–10 in eq 7), which is independent of the calibration procedure

$$\Gamma_{\text{th}} = \frac{8.22 \cdot \rho_{\text{MOF}}}{f_{\text{fit}}} \quad (11)$$

With the theoretical model (Supplementary Note 3.3) and eq 11 at hand, we use the SC isotherm data itself expressed as the ratio  $A_{\text{OH}}/A_{\text{CH}}$  as a function of RH and fit its course to the model function  $N_{\text{H}_2\text{O}}(\text{RH})$  to determine the scaling factor  $\Gamma_{\text{th}}$ . Figure 6f depicts the ratio  $A_{\text{OH}}/A_{\text{CH}}$  at RHs between 0 and  $\sim 77\%$  RH and the model fit function  $N_{\text{H}_2\text{O}}(\text{RH})$  that determines the number of adsorbed water molecules per asymmetric unit cell. We found a model-supported scaling factor  $\Gamma_{\text{th}} = 0.0938 \pm 0.0041$  with uncertainty that only depends on the intrinsic noise of the underlying Raman spectrum (Figure SN3.4). It is in good agreement with the calibration-based scaling factor of  $\Gamma_{\text{exp}} = 0.0837 \pm 0.0131$  (Figure SN3.5) within the range of error (Supplementary Note 3.4).

**Raman-Based SC Isotherms and Sorption Kinetics.** MOF-801 powder was placed in a channel slide ( $\mu$ -Slide I Luer Glass Bottom, Ibbidi) on the microscope and dried under nitrogen flow until a RH of 0.0% was reached (for at least 1 h). In the following, adsorption isotherm/kinetic curves refer to measurements with a prior increase in RH, while desorption experiments refer to a prior decrease in RH. Crystals were selected in the bright-field channel and measured in the midplane of the selected particles. The corresponding measurement parameters are summarized in Table 1. If not mentioned otherwise, the power density at the confocal volume was  $58.5 \text{ mW}/\mu\text{m}^2$  for all

**Table 1. Measurement Setting for SC Sorption Isotherms, SC Kinetics, and Raman Mapping of Water in MOF-801**

measurement mode	integration time (s)	accumulation	EM gain
SC isotherm	50	5	0
SC kinetic	20	1	100
hyperspectral imaging	5	1	100

isotherm experiments and  $67.5 \text{ mW}/\mu\text{m}^2$  for all kinetic experiments (see Supplementary Note 8).

For SC isotherms, we waited for equilibration of the system after a change in RH (at least 3 min) before starting the measurement of each data point. For SC adsorption/desorption isotherms, we waited at least 10 min after the adsorption measurement before reducing the RH again to ensure full saturation with humid air at the upper turning point between adsorption and desorption isotherm.

For monitoring the SC adsorption kinetics, we dried the sample as described above and adjusted the RH in the disconnected wet line meanwhile to 8% RH. At  $t = 0 \text{ s}$ , a kinetic series in the Andor Solis software was started in multitrack mode, and the three-way vault was applied to switch from the dry to the humid flow. The tube length between the vault and channel slide was ca. 80 cm with an inner tube diameter of 2 mm, resulting in ca.  $2.5 \text{ cm}^3$  volume. The channel slide has an inner volume of 60  $\mu\text{L}$ . The constant flow of 1 standard liter/minute (ca. 18 mL/s, i.e., 1080 mL/min for nitrogen at 23.3 °C) ensures a complete air exchange over the sample in less than 1 s. For the designed system and settings, we found that the adsorption kinetics is not dominated by the flow rate (Figure SN4.3). For monitoring the SC desorption kinetics, the sample system was held at a fixed RH, e.g., at 8% RH until  $t = 0 \text{ s}$ . Then, the mass flow controllers were set to 1 and 0 standard liter per minute, effectively exposing the sample with dry nitrogen only under a controlled flow at 1 standard liter per minute. For cycling kinetic experiments, the ratio of the mass flow controllers was alternated every 80 s between dry air only and predefined values (e.g., 0.9 (dry) to 0.1 (humid) standard liter per minute for 8% RH).

**MOF-801 Synthesis. Chemicals.** Zirconium oxychloride octahydrate ( $\text{ZrOCl}_2 \cdot 8\text{H}_2\text{O}$ , purity  $\geq 99.5\%$ ), fumaric acid, and Sigmacote siliconizing reagent were obtained from Sigma-Aldrich Co. *N,N*-Dimethylformamide (DMF), formic acid (purity  $\geq 99.0\%$ ), and anhydrous methanol were obtained from EMD Millipore Chemicals. Anhydrous acetone was obtained from Acros Organics.

**Preparation of Single MOF-801 Crystals.** For synthesizing monocrystalline SC-MOF-801 [ $\text{Zr}_6\text{O}_4(\text{OH})_4(\text{fumarate})_6$ ], fumaric acid (0.027 g, 0.23 mmol) and  $\text{ZrOCl}_2 \cdot 8\text{H}_2\text{O}$  (0.075 g, 0.23 mmol) were dissolved in DMF (11.67 mL) before adding formic acid (1.76 mL) to the solution. The solvent mixture was placed in a 20 mL vial, which was heated at 120 °C for 2 days. Octahedral colorless crystals were collected and washed with fresh DMF three times per day for 3 days. The crystals were subsequently washed with fresh methanol for 3 days, three times per day. The solid was then dried under dynamic vacuum at room temperature for 2 h and at 120 °C for 24 h to yield an activated sample.

**Preparation of MOF-801 as Microcrystalline Powder.** For synthesizing microcrystalline powder of MOF-801 [ $\text{Zr}_6\text{O}_4(\text{OH})_4(\text{fumarate})_6$ ], fumaric acid (0.290 g, 2.50 mmol) and  $\text{ZrOCl}_2 \cdot 8\text{H}_2\text{O}$  (0.805 g, 2.50 mmol) were dissolved in DMF (10.0 mL) before adding formic acid (3.50 mL) to the solution. The solvent mixture was placed in a 20 mL vial and heated at 130 °C for 6 h. The as-synthesized microcrystalline powder was collected and washed with fresh DMF three times per day for 3 days. The sample was then washed with fresh methanol three times per day for 3 days. The solid was afterward dried under dynamic vacuum at room temperature for 2 h and at 120 °C for 24 h to yield an activated sample. To reduce the nucleation in the growth of MOF-801 samples, the inner surface of the 20 mL vial was rinsed with siliconizing reagent Sigmacote, washed with acetone, and dried in the oven before use.

**MOF-801 Characterization. Single-Crystal X-Ray Diffraction.** SC-XRD datasets were collected at the beamline 12.2.1 at the Advanced Light Source (Lawrence Berkeley National Laboratory, USA) using a radiation wavelength of  $\lambda = 0.7288 \text{ \AA}$ . Beamline 12.2.1 is equipped with a PHOTON-II CMOS detector operating in shutterless mode and a Si(111) monochromator. For the measurement, the crystalline sample was mounted on a Kapton MiTeGen MicroMount in a minimal amount of Paratone N oil and submerged in a cold gas stream generated by an Oxford Cryosystems 800 Series Cryostream.



**Scanning Electron Microscopy (SEM).** SEM measurements were carried out on an FEI Quanta 3D FEG scanning electron microscope using an accelerating voltage of 10 kV and a working distance of 10.4 mm. Prior to experiments, crystalline MOF-801 powder was thoroughly washed with DMF and methanol, activated under dynamic vacuum, and afterward dispersed on a silicon wafer.

**Sorption Measurements for Determining Isotherms and Kinetic Curves in Bulk.** Low-pressure  $N_2$  adsorption measurements were carried out on a Micromeritics ASAP 2420 surface area analyzer. Ultrahigh-purity-grade  $N_2$  and He (99.999% purity) were used throughout adsorption experiments. MOF-801 samples were dried under dynamic vacuum at 120 °C for 12 h prior to the analyses. Kinetic water adsorption curves were conducted on 1.029 mg of MOF-801, uniformly distributed on a 6.35 mm diameter pan with the help of a thermogravimetric analyzer under constant humidified nitrogen flow (200 mL  $min^{-1}$ ). The water sorption dynamics measurements were conducted with a TA Instruments SDT Q600 series thermal gravimetric analyzer. The primary gas inlet was directly connected to a nitrogen tank (Praxair, ultrahigh purity, 99.999%). The secondary gas inlet was used to supply a humidified nitrogen feed by regulating the gas flow using a mass flow controller (Sierra SmartTrak 100) and passing the stream through a gas washing bottle (2 L). The temperature and RH were monitored using high-accuracy thermocouples and humidity sensors downstream of the TGA chamber. For the measurements in thin-layer geometry, ~1 mg of the microcrystalline powder sample of MOF-801 was loaded in the TGA pan. Prior to the adsorption measurement in the TGA, the microcrystalline MOF-801 sample was activated under dry nitrogen flow (176 mL  $min^{-1}$ ) at 150 °C, respectively, until the weights of MOFs do not have noticeable changes. After activation, the samples were cooled down to 30 °C under dry nitrogen flow (176 mL  $min^{-1}$ ). Immediately after 30 °C was reached, the adsorption measurement was started. The temperature during the adsorption was kept constant at 30 °C, and the RH was kept at 8%.

**Correlative FWM and CARS Imaging for Probing Water inside MOF-801.** The water distribution between MOF-801 crystals was visualized by multimodal imaging using two microscopy techniques: FWM and CARS. For this, we previously coupled a pulsed near-infrared light source in a home-built scanning Raman microscope.<sup>26</sup> Briefly, two synchronized femtosecond laser pulse trains at  $\omega_1 = 774$  nm and  $\omega_2 = 1053$  nm serve to derive the pump and Stokes beams as third-order nonlinear excitation. The pump beam at 774 nm has a pulse duration of about 150 fs. The spectrally broadened Stokes beam was derived by super-continuum generation in a PCF at 1053 nm. Both pulse trains were recombined and coupled into the scanning microscope collinearly with the CW laser. The details on optical elements controlling the chirp, polarization, intensity, and beam shape have been outlined previously.<sup>26</sup> At given temporal and spatial overlap between both excitation sources within the MOF-801 sample, a nonlinear resonance at  $2\omega_1 - \omega_2$  can be detected in epi-direction by decoupling the signal from the excitation via a dichroic mirror (zt532/NIRrpc; AHF, Germany) and spectral filtering via a bandpass filter (HQ 620/60 M; AHF, Germany) before avalanche photodiodes (Count Red; LaserComponents). Scanning of the sample is achieved using an XYZ piezo stage (BIO3.200; PiezoConcept).

FWM is a third-order nonlinear process that occurs independently of molecular transitions present in the sample. In the presence of a vibrational or electronic resonance, the FWM signal is strongly enhanced and dominated by either coherent Raman scattering (CARS) or stimulated parametric emission, respectively. We employed polarization-dependent CARS (pCARS) to separate the vibrational response of the material from the unspecific FWM background by tuning the relative polarization angle between the linearly polarized excitation beams. An additional polarizer in front of the detector allows for selecting between CARS and FWM signals. To address the OH stretch band around 3400  $cm^{-1}$ , we made use of spectral focusing by chirping the Stokes beam within a 20 cm SF6 glass rod and temporally overlapping the pump beam with the corresponding spectral components of the Stokes beam.<sup>26</sup> FWM

microscopy at ~612 nm used the temporal overlap with non-resonant components around 1050 nm.

Scan times per image were 180 s with an average power density of 26.7 and 59.5  $mW/\mu m^2$  at the confocal volume for pump and Stokes pulses, respectively. CARS and FWM images were scanned with 500 × 500 pixels and a step size of 180  $\mu m$  and accumulated over 3 repeats.

## ■ ASSOCIATED CONTENT

### Supporting Information

The Supporting Information is available free of charge at <https://pubs.acs.org/doi/10.1021/jacs.3c02902>.

Summary of the uptake mechanism in MOF-801 and the implemented fit model for monitoring the uptake of water as function of time or humidity, detailed description and derivation for quantitative monitoring of water uptake by Raman spectroscopy, impact of various experimental parameter on SC measurements, results on polycrystalline MOF-801 particles characterized by SC-XRD and their performance in cyclic water uptake, and adsorption capability of MOF-801 to water in the presence of  $D_2O$  (PDF)

## ■ AUTHOR INFORMATION

### Corresponding Authors

**Omar M. Yaghi** – Department of Chemistry and Kavli Energy Nanoscience Institute and Bakar Institute of Digital Materials for the Planet, Division of Computing, Data Science, and Society, University of California–Berkeley, Berkeley, California 94720, United States; UC Berkeley-KACST Joint Center of Excellence for Nanomaterials for Clean Energy Applications, King Abdulaziz City for Science and Technology, Riyadh 11442, Saudi Arabia; [orcid.org/0000-0002-5611-3325](https://orcid.org/0000-0002-5611-3325); Email: [yaghi@berkeley.edu](mailto:yaghi@berkeley.edu)

**Evelyn Ploetz** – Department of Chemistry and Center for NanoScience (CeNS), Ludwig-Maximilians-Universität München, 81377 Munich, Germany; [orcid.org/0000-0003-0922-875X](https://orcid.org/0000-0003-0922-875X); Email: [evelyn.ploetz@lmu.de](mailto:evelyn.ploetz@lmu.de)

### Authors

**Adrian Fuchs** – Department of Chemistry and Center for NanoScience (CeNS), Ludwig-Maximilians-Universität München, 81377 Munich, Germany

**Fabian Knechtel** – Department of Chemistry and Center for NanoScience (CeNS), Ludwig-Maximilians-Universität München, 81377 Munich, Germany

**Haoze Wang** – Department of Chemistry and Kavli Energy Nanoscience Institute, University of California–Berkeley, Berkeley, California 94720, United States

**Zhe Ji** – Department of Chemistry and Kavli Energy Nanoscience Institute, University of California–Berkeley, Berkeley, California 94720, United States; Present Address: Department of Chemistry, Stanford University, Stanford, California 94305, United States (Z.J.); [orcid.org/0000-0002-8532-333X](https://orcid.org/0000-0002-8532-333X)

**Stefan Wuttke** – BCMaterials, Basque Center for Materials, 48940 Leioa, Spain; Ikerbasque, Basque Foundation for Science, 48013 Bilbao, Spain; [orcid.org/0000-0002-6344-5782](https://orcid.org/0000-0002-6344-5782)

Complete contact information is available at: <https://pubs.acs.org/doi/10.1021/jacs.3c02902>

## Author Contributions

<sup>○</sup>A.F. and F.K. contributed equally.

## Notes

The authors declare no competing financial interest.

## ACKNOWLEDGMENTS

Funding by the Center for NanoScience Munich (CeNS), the Center for Integrated Protein Science Munich (CiPSM), Nanosystems Initiative Munich (NIM), and the Deutsche Forschungsgemeinschaft (PL 696/4-1; Project-ID 201269156-SFB1032, B03) is gratefully acknowledged. We thank Don C. Lamb for support and access to laboratory facilities. These sorption experiments on bulk material are based on work supported by the Defense Advanced Research Projects Agency (DARPA) under contract HR001-21-C0020. Any opinions, findings, and conclusions or recommendations expressed in this material are those of the author(s) and do not necessarily reflect the views of DARPA. Experimental support by Ludwig Steidl and Sofia Feldl, who helped in setting up measurements under controlled RH, and Nikita Hanikel, who carried out the sorption experiments in bulk, are greatly acknowledged.

## ABBREVIATIONS

AWH	atmospheric water harvesting
BF	bright-field
CARS	coherent anti-Stokes Raman scattering
FWM	four-wave mixing
HRI	hyperspectral Raman imaging
MOF	metal-organic framework
RH	relative humidity
SC	single crystal
WHC	water harvesting cycling

## REFERENCES

- (1) Chae, H. K.; Siberio-Pérez, D. Y.; Kim, J.; Go, Y.; Eddaoudi, M.; Matzger, A. J.; O'Keeffe, M.; Yaghi, O. M.; Materials, D.; Discovery, G. A route to high surface area, porosity and inclusion of large molecules in crystals. *Nature* **2004**, *427*, 523–527.
- (2) Furukawa, H.; Gandara, F.; Zhang, Y. B.; Jiang, J.; Queen, W. L.; Hudson, M. R.; Yaghi, O. M. Water adsorption in porous metal-organic frameworks and related materials. *J. Am. Chem. Soc.* **2014**, *136*, 4369–4381.
- (3) Hanikel, N.; Pei, X.; Chheda, S.; Lyu, H.; Jeong, W.; Sauer, J.; Gagliardi, L.; Yaghi, O. M. Evolution of water structures in metal-organic frameworks for improved atmospheric water harvesting. *Science* **2021**, *374*, 454–459.
- (4) Kim, H.; Rao, S. R.; Kapustin, E. A.; Zhao, L.; Yang, S.; Yaghi, O. M.; Wang, E. N. Adsorption-based atmospheric water harvesting device for arid climates. *Nat. Commun.* **2018**, *9*, 1191.
- (5) LaPotin, A.; Zhong, Y.; Zhang, L.; Zhao, L.; Leroy, A.; Kim, H.; Rao, S. R.; Wang, E. N. Dual-Stage Atmospheric Water Harvesting Device for Scalable Solar-Driven Water Production. *Joule* **2021**, *5*, 166–182.
- (6) Logan, M. W.; Langevin, S.; Xia, Z. Reversible Atmospheric Water Harvesting Using Metal-Organic Frameworks. *Sci. Rep.* **2020**, *10*, 1492.
- (7) Wang, W.; Xie, S.; Pan, Q.; Dai, Y.; Wang, R.; Ge, T. Air-cooled adsorption-based device for harvesting water from island air. *Renewable Sustainable Energy Rev.* **2021**, *141*, No. 110802.
- (8) Xu, W.; Yaghi, O. M. Metal-Organic Frameworks for Water Harvesting from Air, Anywhere, Anytime. *ACS Cent. Sci.* **2020**, *6*, 1348–1354.
- (9) Zhang, L.; Fang, W.-X.; Wang, C.; Dong, H.; Ma, S.-H.; Luo, Y.-H. Porous frameworks for effective water adsorption: from 3D bulk to 2D nanosheets. *Inorg. Chem. Front.* **2021**, *8*, 898–913.
- (10) Zhou, X.; Lu, H.; Zhao, F.; Yu, G. Atmospheric Water Harvesting: A Review of Material and Structural Designs. *ACS Mater. Lett.* **2020**, *2*, 671–684.
- (11) Kim, H.; Yang, S.; Rao, S. R.; Narayanan, S.; Kapustin, E. A.; Furukawa, H.; Umans, A. S.; Yaghi, O. M.; Wang, E. N. Water harvesting from air with metal-organic frameworks powered by natural sunlight. *Science* **2017**, *356*, 430.
- (12) Hanikel, N.; Prévot, M. S.; Fathieh, F.; Kapustin, E. A.; Lyu, H.; Wang, H.; Diercks, N. J.; Glover, T. G.; Yaghi, O. M. Rapid Cycling and Exceptional Yield in a Metal-Organic Framework Water Harvester. *ACS Cent. Sci.* **2019**, *5*, 1699–1706.
- (13) Hossain, M. I.; Glover, T. G. Kinetics of Water Adsorption in UiO-66 MOF. *Ind. Eng. Chem. Res.* **2019**, *58*, 10550–10558.
- (14) Solovyeva, M. V.; Gordeeva, L. G.; Krieger, T. A.; Aristov, Y. I. MOF-801 as a promising material for adsorption cooling: Equilibrium and dynamics of water adsorption. *Energy Convers. Manage.* **2018**, *174*, 356–363.
- (15) Liu, X.; Wang, X.; Kapteijn, F. Water and Metal-Organic Frameworks: From Interaction toward Utilization. *Chem. Rev.* **2020**, *120*, 8303–8377.
- (16) Bagi, S.; Wright, A. M.; Oppenheim, J.; Dincă, M.; Román-Leshkov, Y. Accelerated Synthesis of a Ni<sub>2</sub>Cl<sub>2</sub>(BTDD) Metal-Organic Framework in a Continuous Flow Reactor for Atmospheric Water Capture. *ACS Sustainable Chem. Eng.* **2021**, *9*, 3996–4003.
- (17) Bagi, S.; Yuan, S.; Rojas-Buzo, S.; Shao-Horn, Y.; Román-Leshkov, Y. A continuous flow chemistry approach for the ultrafast and low-cost synthesis of MOF-808. *Green Chem.* **2021**, *23*, 9982–9991.
- (18) Bon, V.; Senkovska, I.; Evans, J. D.; Wöllner, M.; Hölzel, M.; Kaskel, S. Insights into the water adsorption mechanism in the chemically stable zirconium-based MOF DUT-67 – a prospective material for adsorption-driven heat transformations. *J. Mater. Chem. A* **2019**, *7*, 12681–12690.
- (19) Towsif Abtab, S. M.; Alezi, D.; Bhatt, P. M.; Shkurenko, A.; Belmabkhout, Y.; Aggarwal, H.; Weseliński, Ł. J.; Alsadun, N.; Samin, U.; Hedhili, M. N.; et al. Reticular Chemistry in Action: A Hydrolytically Stable MOF Capturing Twice Its Weight in Adsorbed Water. *Chem* **2018**, *4*, 94–105.
- (20) LaPotin, A.; Kim, H.; Rao, S. R.; Wang, E. N. Adsorption-Based Atmospheric Water Harvesting: Impact of Material and Component Properties on System-Level Performance. *Acc. Chem. Res.* **2019**, *52*, 1588–1597.
- (21) Mallamace, F.; Branca, C.; Broccio, M.; Corsaro, C.; Mou, C. Y.; Chen, S. H. The anomalous behavior of the density of water in the range 30 K < T < 373 K. *Proc. Natl. Acad. Sci. U. S. A.* **2007**, *104*, 18387–18391.
- (22) Huang, X. F.; Wang, Q.; Liu, X. X.; Yang, S. H.; Li, C. X.; Sun, G.; Pan, L. Q.; Lu, K. Q. Vibrational Dynamics of Water within Mesoporous Materials at Different Hydration Levels during Adsorption and Desorption Processes. *J. Phys. Chem. C* **2009**, *113*, 18768–18771.
- (23) Rieth, A. J.; Hunter, K. M.; Dincă, M.; Paesani, F. Hydrogen bonding structure of confined water templated by a metal-organic framework with open metal sites. *Nat. Commun.* **2019**, *10*, 4771.
- (24) Avrami, M. Kinetics of Phase Change. II Transformation-Time Relations for Random Distribution of Nuclei. *J. Chem. Phys.* **1940**, *8*, 212–224.
- (25) Guo, B.; Wang, Y.; Shen, X.; Qiao, X.; Jia, L.; Xiang, J.; Jin, Y. Study on CO(2) Capture Characteristics and Kinetics of Modified Potassium-Based Adsorbents. *Materials* **2020**, *13*, 877.
- (26) Fuchs, A.; Mannhardt, P.; Hirschle, P.; Wang, H.; Zaytseva, I.; Ji, Z.; Yaghi, O. M.; Wuttke, S.; Ploetz, E. Single Crystals Heterogeneity Impacts the Intrinsic and Extrinsic Properties of Metal-Organic Frameworks. *Adv. Mater.* **2022**, *34*, No. 2104530.
- (27) Müller, K.; Vankova, N.; Schöttner, L.; Heine, T.; Heinke, L. Dissolving uptake-hindering surface defects in metal-organic frameworks. *Chem. Sci.* **2019**, *10*, 153–160.

(28) Fathieh, F.; Kalmutzki, M. J.; Kapustin, E. A.; Waller, P. J.; Yang, J.; Yaghi, O. M. Practical water production from desert air. *Sci. Adv.* **2018**, *4*, No. eaat3198.

(29) Terzis, A.; Ramachandran, A.; Wang, K.; Asheghi, M.; Goodson, K. E.; Santiago, J. G. High-Frequency Water Vapor Sorption Cycling Using Fluidization of Metal-Organic Frameworks. *Cell Rep. Phys. Sci.* **2020**, *1*, No. 100057.

(30) Delen, G.; Monai, M.; Meirer, F.; Weckhuysen, B. M. In situ Nanoscale Infrared Spectroscopy of Water Adsorption on Nanoislands of Surface-Anchored Metal-Organic Frameworks. *Angew. Chem., Int. Ed.* **2021**, *60*, 1620–1624.

## Recommended by ACS

### Simultaneous Control of Flexibility and Rigidity in Pore-Space-Partitioned Metal–Organic Frameworks

Yuchen Xiao, Pingyun Feng, *et al.*

MAY 10, 2023  
JOURNAL OF THE AMERICAN CHEMICAL SOCIETY

READ 

### High-Concentration Self-Assembly of Zirconium- and Hafnium-Based Metal–Organic Materials

Ronald T. Jerozal, Phillip J. Milner, *et al.*

JUNE 09, 2023  
JOURNAL OF THE AMERICAN CHEMICAL SOCIETY

READ 

### Stepwise Assembly of Quinary Multivariate Metal–Organic Frameworks via Diversified Linker Exchange and Installation

Yuchen Hu, Jian Zhang, *et al.*

JUNE 15, 2023  
JOURNAL OF THE AMERICAN CHEMICAL SOCIETY

READ 

### Dynamic Bond-Directed Synthesis of Stable Mesoporous Metal–Organic Frameworks under Room Temperature

Youcong Li, Jing-Lin Zuo, *et al.*

APRIL 19, 2023  
JOURNAL OF THE AMERICAN CHEMICAL SOCIETY

READ 

Get More Suggestions >